

# Three-dimensional Atomic Mapping of Ligands on Nanoparticles

*Kyuseon Jang,<sup>+,†</sup> Se-Ho Kim,<sup>+,†,§</sup> Hosun Jun,<sup>†</sup> Chanwon Jung,<sup>†</sup> Jiwon Yu,<sup>‡</sup> Sangheon Lee,<sup>\*,‡</sup>*

*Pyuck-Pa Choi<sup>\*,†</sup>*

<sup>†</sup>Department of Materials Science and Engineering, Korea Advanced Institute of Science and Technology (KAIST), 291 Daehak-ro, Yuseong-gu, Daejeon 34141, Republic of Korea

<sup>§</sup>Department of Microstructure Physics and Alloy Design, Max-Planck-Institut für Eisenforschung GmbH, Max-Planck-Straße 1, 40237, Düsseldorf, Germany

<sup>‡</sup>Department of Chemical Engineering and Materials Science, Ewha Womans University, 52, Ewhayeodae-gil, Seodaemun-gu, Seoul 03760, Republic of Korea

[<sup>+</sup>] These authors contributed equally to this work.

[\*] Co-corresponding authors

KEYWORDS: multiple twinned nanoparticle, halide ion, surfactant, oxidative etching, atom probe tomography

## Abstract

Capping ligands are crucial to synthesize colloidal nanoparticles with novel functional properties. However, the interaction between capping ligands and their interaction with the crystallographic surfaces of nanoparticles during colloidal synthesis remains a great mystery, due to the lack of direct imaging techniques. In this study, atom probe tomography was adopted to investigate the three-dimensional atomic-scale distribution of two of the most common types of these ligands, cetrimonium and halide (Br and Cl) ions, on Pd nanoparticles. The results, validated using the density functional theory, demonstrated that the Br anions adsorbed on the nanoparticle surfaces promote the adsorption of the cetrimonium cations through electrostatic interactions, stabilizing the Pd {111} facets. In contrast, the Cl anions were not strongly adsorbed onto the Pd surfaces. The high density of adsorbed cetrimonium cations for Br anion additions resulted in the formation of multiple-twinned nanoparticles with superior oxidation resistance.

## Introduction

More than three decades of intensive research have fundamentally changed the perception of nanomaterials. What started as a scientific curiosity has led to novel materials, which are now used in real-world applications and have become essential for our everyday life. The research on nanomaterials was largely driven by their intriguing physical and chemical properties, such as the outstanding luminescence of semiconductor nanocrystals<sup>1</sup>, the excellent energy storage performance of two-dimensional nanosheets<sup>2</sup>, and the remarkable catalytic activity and selectivity of noble metal nanocatalysts<sup>3,4</sup>. These properties are usually ascribed to the limited size and high surface-to-volume ratio of nanomaterials, compared with their bulk counterparts.

Among the several nanomaterials reported to date, colloidal nanoparticles (NPs) are particularly attractive since they can be synthesized in large quantities at reasonable costs and their size, shape, and properties can be carefully tailored through optimized growth recipes<sup>5</sup>. Colloidal NPs are nowadays deployed on an industrial scale in key technological fields such as catalysis<sup>6</sup>, energy conversion<sup>7</sup>, and optoelectronics<sup>8</sup>.

Various methods have been developed for synthesizing colloidal NP, including hydrothermal synthesis<sup>9</sup>, polyol synthesis<sup>10</sup>, microemulsion technique<sup>11</sup>, and sol–gel process<sup>12</sup>. Although each of these methods is unique, they share a common feature, i.e., they all rely on capping ligands. Capping ligands are additives adsorbed on specific crystallographic surfaces of the NPs; they can prevent NP agglomeration and control the NP size, shape, and functionality<sup>13–15</sup>. Therefore, capping ligands are paramount to tune the properties of colloidal NPs<sup>16</sup>. The most used capping ligands are thiols, block copolymers, cetrimonium, and halide ions<sup>17</sup>; the latter two are particularly advantageous as they can be applied in various nanoparticle systems<sup>17</sup>.

Although capping ligands are indispensable for synthesizing colloidal NPs, little is known about their adsorption behavior on different crystallographic facets, especially at the atomic scale.

There are still some important unanswered questions: What are the amounts of ligand molecules adsorbed on the NP surfaces? What is the interplay between different ligands added together during a growth process? How do ligands stabilize the NP surfaces thermodynamically and kinetically? How do ligands influence the inherent vulnerability of the NP surfaces against chemical attack?

While there have been advances in analyzing capping ligands via nuclear magnetic resonance spectroscopy<sup>18</sup>, scanning tunneling microscopy<sup>19,20</sup>, transmission electron microscopy (TEM)<sup>21,22</sup>, Fourier-transform infrared (FT-IR) spectroscopy<sup>23</sup>, and computational simulations<sup>24</sup>, the direct mapping of the three-dimensional (3D) distribution, as well as the quantification of the ligands on the NPs remains a great challenge. The lack of experimental data is attributed to limited spatial resolution and/or detection sensitivity of many of the analytical techniques used<sup>25</sup>.

Atom probe tomography (APT) is an advanced technique that can overcome such limitations<sup>26</sup>. Its principle is based on the field evaporation of atoms from a needle-shaped specimen cryogenically cooled under ultrahigh vacuum and subjected to an intense electric field ( $\sim 10\text{--}50\text{ V/nm}$ ). The specimen atoms undergo ionization during the field evaporation process; the resulting ions are accelerated by electrostatic forces toward a position-sensitive detector that measures their time-of-flight and impact coordinates, which are used for calculating a mass spectrum and reconstructing a 3D atom map, respectively.

The unique combination of near-atomic resolution and ppm-level detection sensitivity, irrespective of the elemental mass, makes APT an ideal tool for the characterization of nanomaterials. Therefore, we adopted this state-of-the-art technique to investigate the 3D distribution of cetrimonium ligands on multiple-twinned NPs (MTNPs) of Pd, which are

promising nanocatalysts for technologically important chemical reactions, such as oxygen reduction and formic acid oxidation, but are prone to oxidative etching<sup>27,28</sup>.

In this work, we could synthesize highly stable Pd MTNPs via the simple reduction of a precursor in an aqueous solution by adding both cetrimonium cations ( $C_{19}H_{42}N^+$ , denoted as  $CTA^+$  in the following) and Br anions. However, we also observed that replacing the Br anions with Cl anions reduced the yield of Pd MTNPs and led to substantial oxidative etching of their surfaces; to understand this peculiar behavior, we analyzed the distribution of  $CTA^+$  on the Pd NPs via APT and could directly attribute the formation of multiple-twinned structures and the oxidation resistance of the NP specimens to their surface coverage by  $CTA^+$ . To validate and support the experimental data, we calculated the binding energy of the ligands on various Pd NP facets by using the *ab initio* density functional theory (DFT). We could demonstrate that the complex interplay between Pd NP surfaces, ligand ions, and solvent determines the shape and oxidative etching resistance of the final nanoparticles.

## Results

**Structural characterization.** Figure 1 shows the TEM images of the Pd NPs synthesized by adding  $Br^-$  or  $Cl^-$  additions (hereafter, denoted as  $Pd_{(Br)}$  and  $Pd_{(Cl)}$  NPs, respectively). The  $Pd_{(Br)}$  NPs mainly exhibited either icosahedral or decahedral (Fig. 1a and Supplementary Fig. 1) multiple-twinned structures, as confirmed via high-resolution TEM (HRTEM) and fast Fourier transform (FFT) imaging (see Fig. 1b for an icosahedral MTNP); all the facets showed a lattice spacing of 0.222 nm, corresponding to the interplanar spacing of the  $\{111\}$  planes (Fig. 1b)<sup>29</sup>.

The MTNPs accounted for about 80% of the  $Pd_{(Br)}$  NP batch, while the rest included minor products such as single-twinned right bipyramids, cubes, nanorods, and tetrahedra. The

icosahedral NPs exhibited a smaller average size ( $19 \pm 1$  nm) than the decahedral ones ( $24 \pm 1$  nm); this result agrees with previous computational studies predicting that decahedra tend to form larger particles than icosahedra due to the more abundant twin boundaries of the latter and the correspondingly higher lattice strain energy<sup>30</sup>.

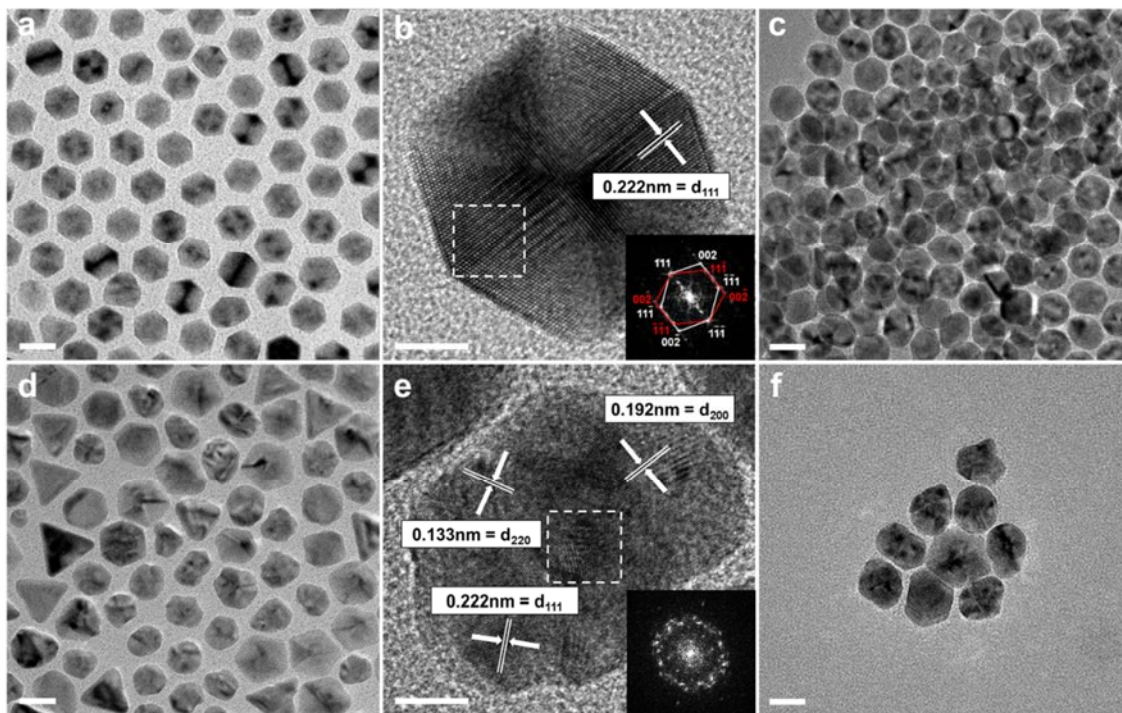


**Fig. 1** Transmission electron microscopy (TEM) images of the synthesized Pd nanoparticles (NPs). **a–c** Multiple-twinned NPs produced by adding Br anions: **a**, **b** As-synthesized and **c** washed nanoparticles after exposure to air for ten days. **d–f** NPs produced by adding Cl anions: **d**, **e** As-synthesized and **f** washed nanoparticles after exposure to air for ten days. The insets in **b** and **e** show the fast Fourier transform patterns corresponding to the white dotted line areas. (Scale bars: 20 nm in **a**, **c**, **d**, **f** and 5 nm in **b**, **e**)

Although twin boundaries with numerous active sites can enhance the catalytic properties of MTNPs, they seem also prone to oxidative dissolution<sup>31,32</sup>. Thus, the synthesis and the storage of MTNPs in oxidative environments, such as air or aqueous solutions, are challenging<sup>33</sup>.

However, in this work, we made some unexpected observations for the Pd<sub>(Br)</sub> MTNPs. First, most of them did not undergo any remarkable oxidative dissolution although they were synthesized in an oxidative environment, i.e., in an aqueous solution at near-boiling temperature (90 °C) for 48 h in air. Moreover, they were largely preserved even after long-term storage in an oxidative environment, as discussed below. Besides, most of the Pd<sub>(Br)</sub> NPs exhibited only {111} facets, although Br anions were previously reported to promote the formation of {100} facets in Pd<sup>34,35</sup>.

Unlike the Pd<sub>(Br)</sub> NPs, the Pd<sub>(Cl)</sub> NPs were mainly round-cornered cuboctahedra and tetrahedra (Fig. 1d,e), many of which showed strongly distorted shapes. Only about 30% of the Pd<sub>(Cl)</sub> NPs were MTNPs, whose corners and edges were rounder than those of the Pd<sub>(Br)</sub> MTNPs. Figure 1e shows an HRTEM and an FFT image of a Pd<sub>(Cl)</sub> NP having distorted shape, with no multiple-twinned structures; besides {111} facets, this distorted NP exhibited also {220} and {200} facets<sup>36</sup>. These observations indicate that the Pd<sub>(Cl)</sub> MTNPs underwent oxidative etching during their synthesis, while the Pd<sub>(Br)</sub> MTNPs were little affected by such a phenomenon.

To further compare the resistance of the two NP batches against oxidative etching, we washed the Pd<sub>(Br)</sub> and Pd<sub>(Cl)</sub> colloidal specimens to remove excess CTA<sup>+</sup> and stored them at room temperature in air for ten days. Since the Pd<sub>(Cl)</sub> NPs were exposed to a higher concentration of Cl<sup>-</sup> than the Pd<sub>(Br)</sub> ones during their synthesis, we added KCl to the Pd<sub>(Br)</sub> specimen before storage to match the amount of Cl anions acting as an etchant<sup>35</sup>. As shown in Fig. 1c and Supplementary Fig. 2a, the Pd<sub>(Br)</sub> MTNPs retained most of their twin boundaries, showing slightly rounded vertices due to oxidative etching. Compared to previous studies, where the MTNPs were completely dissolved during synthesis in air<sup>37</sup>, these Pd<sub>(Br)</sub> MTNPs exhibited remarkable stability against oxidative etching even for the tested long-term exposure to an oxidative environment. In contrast, less than 15% of the Pd<sub>(Cl)</sub> NPs were preserved (Fig. 1f and Supplementary Fig. 2b).

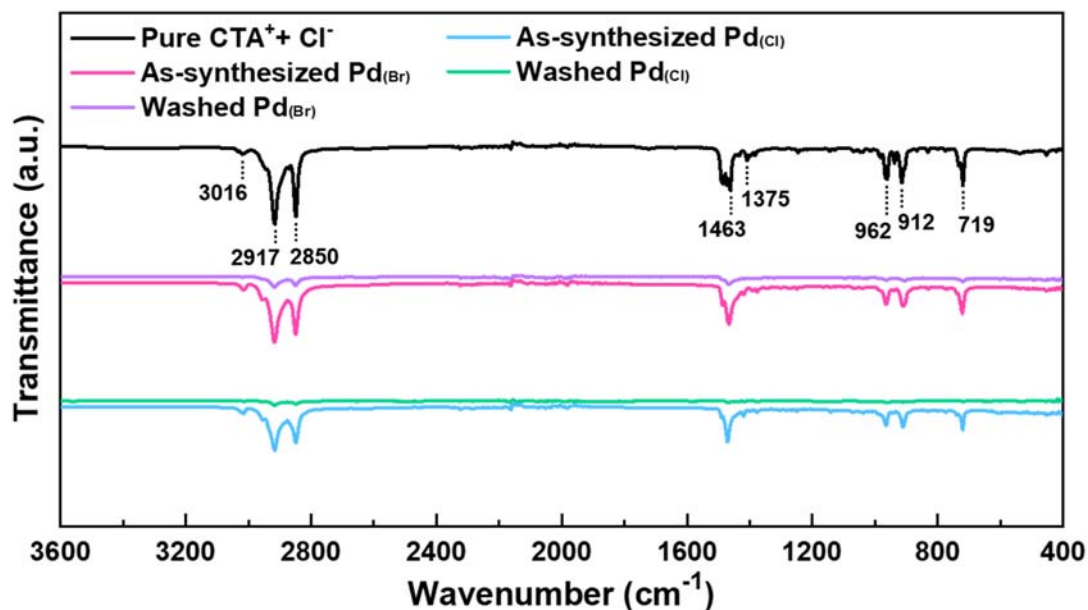


**Fig. 2 Fourier-transform infrared (FT-IR) spectra.** Pure cetrimonium ions ( $\text{CTA}^+$ ) and  $\text{Cl}^-$  anions, compared with Pd nanoparticles produced by adding Br or Cl anions ( $\text{Pd}_{(\text{Br})}$  and  $\text{Pd}_{(\text{Cl})}$ , respectively), as-synthesized and after washing to remove excess  $\text{CTA}^+$ .

To determine whether these results were related to the varying amounts of adsorbed  $\text{CTA}^+$ , depending on the halide ion ligand ( $\text{Br}^-$  or  $\text{Cl}^-$ ) used, we also performed an FT-IR spectroscopy analysis. A reference  $\text{CTA}^+/\text{Cl}^-$  specimen and the as-synthesized  $\text{Pd}_{(\text{Br})}$  and  $\text{Pd}_{(\text{Cl})}$  NPs, before and after a washing process for removing excess  $\text{CTA}^+$  in the solutions, were analyzed (Fig. 2). The FT-IR spectra of both as-synthesized specimens exhibited several peaks related to the  $\text{CTA}^+$ ; the peaks at 3016, 1463, and 1375  $\text{cm}^{-1}$  were due to the asymmetric  $-\text{CH}_3$  stretching bands, while those at 2917 and 2850  $\text{cm}^{-1}$  corresponded to the asymmetric  $-\text{CH}_2-$  stretching bands. Furthermore, the peak at 719  $\text{cm}^{-1}$  was assigned to the  $-\text{CH}_2-$  rock vibration<sup>38</sup> and those at 962 and 912  $\text{cm}^{-1}$  were attributed to the  $-\text{CN}-$  vibration of the cationic head of the  $\text{CTA}^+$ <sup>38</sup>.



After washing the samples by centrifugation, the intensity of all the CTA<sup>+</sup>-related peaks decreased by about 90%. However, the FT-IR data revealed the presence of residual CTA<sup>+</sup> on both the Pd<sub>(Br)</sub> and Pd<sub>(Cl)</sub> NPs even after washing; their amount was higher in the former ones.

**3D distribution and concentration of CTA<sup>+</sup> ligands on the Pd NPs.** We conducted APT measurements on washed Pd<sub>(Br)</sub> and Pd<sub>(Cl)</sub> NPs to reveal the 3D distribution and concentration of CTA<sup>+</sup> on their surfaces. For this analysis, we embedded the NPs in an electrodeposited Ni film via the method described in Refs.<sup>39,40</sup>; then, needle-shaped specimens were obtained from this composite Pd NP–Ni film through focused ion beam (FIB) milling<sup>41</sup>.

Supplementary Fig. 3 and 4 show the mass spectra derived from the APT measurements of the as-prepared Pd<sub>(Br)</sub> and Pd<sub>(Cl)</sub> specimens, respectively. In both cases, the major isotope peaks were assigned to the Pd NPs and Ni in single- and double-charged states. NiH<sup>+</sup> and NiO<sup>+</sup> peaks were detected as well, possibly due to the presence of residual H<sub>2</sub> in the APT analysis chamber and slight oxidation of the Ni film. We detected also C<sup>+</sup>, N<sup>+</sup>, C<sub>2</sub><sup>+</sup>, C<sub>3</sub><sup>+</sup>, and C<sub>4</sub><sup>+</sup> at 12, 14, 24, 36, and 48 Da, respectively. Moreover, other peaks were observed at 42, 43, and 44 Da, assigned to C<sub>2</sub>H<sub>x</sub>N<sup>+</sup><sup>42,43</sup>. The spectrum of the Pd<sub>(Cl)</sub> specimen showed additional peaks between 80 and 100 Da, which could be assigned to complexes of Ni, C, and O, such as NiC<sub>x</sub> and NiO<sub>x</sub>. To determine the amount of C or N impurities introduced from the electrodeposition process, we analyzed also bare electrodeposited Ni films; since the measured average concentrations of C and N were only 0.010 ± 0.005 at% and 0.012 ± 0.003 at% (about 100 times lower than in the Pd-containing specimens), respectively, and there were no other sources of C and N during the NP synthesis (Supplementary Fig. 5), we attributed the C- and N-related peaks detected in the Pd specimens to the CTA<sup>+</sup> ions. Low concentrations (< 0.1 at%) of Cl<sup>+</sup> were detected at 35 and 37 Da in the Pd<sub>(Br)</sub> and Pd<sub>(Cl)</sub> specimens, but the expected Br<sup>+</sup> (79 and 81 Da) and Br<sup>2+</sup> (39.5

and 40.5 Da) signals were below the detection limit for the Pd<sub>(Br)</sub> specimen. This difference in the concentration levels can be ascribed to the fact that Cl was present in three reagents (K<sub>2</sub>PdCl<sub>4</sub>, as the precursor for Pd NPs, cetrimonium chloride, and KCl ligands; see the Methods section) while Br only in one reagent (KBr).

Figure 3a illustrates an APT reconstruction containing two Pd<sub>(Br)</sub> NPs embedded in Ni, along with an isoconcentration surface of 1.5 at% C. At the reconstructed Pd/Ni interface, the C concentration was about 3 at%; the C atoms were detected on the surfaces of both the top and bottom Pd NPs. The 10 nm thin slice viewed along the z-axis shown in Fig. 3b reveals a nearly pentagonal projection for the top Pd NP, suggesting that it is an MTNP with a decahedral shape. The bottom Pd NP, which was partly detected, exhibited a corner, as shown in the slice viewed along the x-axis displayed in Fig. 3c. Both Pd NPs showed segregation of C and N atoms at their surfaces. Supplementary Fig. 6 illustrates another APT dataset where a part of a Pd NP, fully covered by C, was detected.

One CTA<sup>+</sup> (C<sub>19</sub>H<sub>42</sub>N<sup>+</sup>) consists of one N atom bonded to three methyl- and one hexadecyl-carbon group, resulting in a N:C ratio of 1:19. The bulk composition of the C-complex region, marked by the C isoconcentration surface, showed a N:C ratio of 1:18.4, confirming that the C and N atoms indeed originated from the CTA<sup>+</sup>. Thus, these APT results indicate the segregation of CTA<sup>+</sup> on the surface of the Pd<sub>(Br)</sub> NPs.

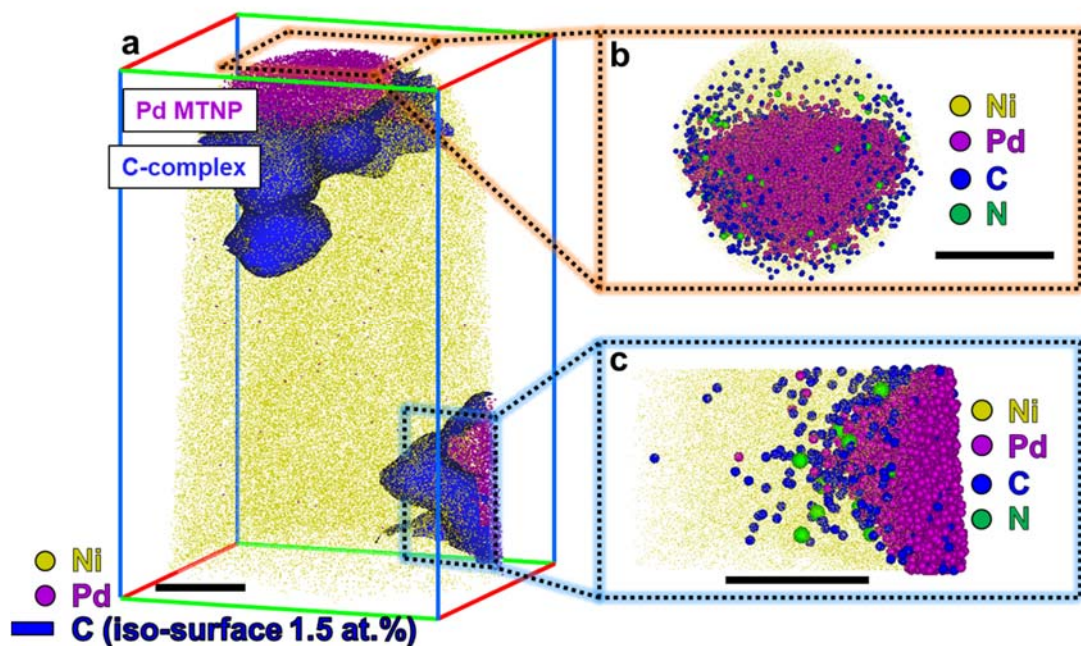


**Fig. 3** Atom probe tomography (APT) reconstruction of Pd multiple-twinned nanoparticles (MTNPs), synthesized by adding Br anions, embedded in Ni. **a** Three-dimensional atom map of Pd atoms and isoconcentration (1.5 at.%) surfaces of C. **b**, **c** Slices viewed along the Pd MTNPs. (Scale bars: 10 nm)

Figure 4a displays a reconstructed 3D atom map of three Pd<sub>(Cl)</sub> NPs in Ni, along with an isoconcentration surface of 3 at% C. Unlike the Pd<sub>(Br)</sub> NPs, the C atoms were detected not only at the Pd surface but also deep within the Ni matrix, i.e., about 10 nanometers away from the Pd<sub>(Cl)</sub> NPs (Fig. 4b, c). Similar results were observed for the Cl atoms.

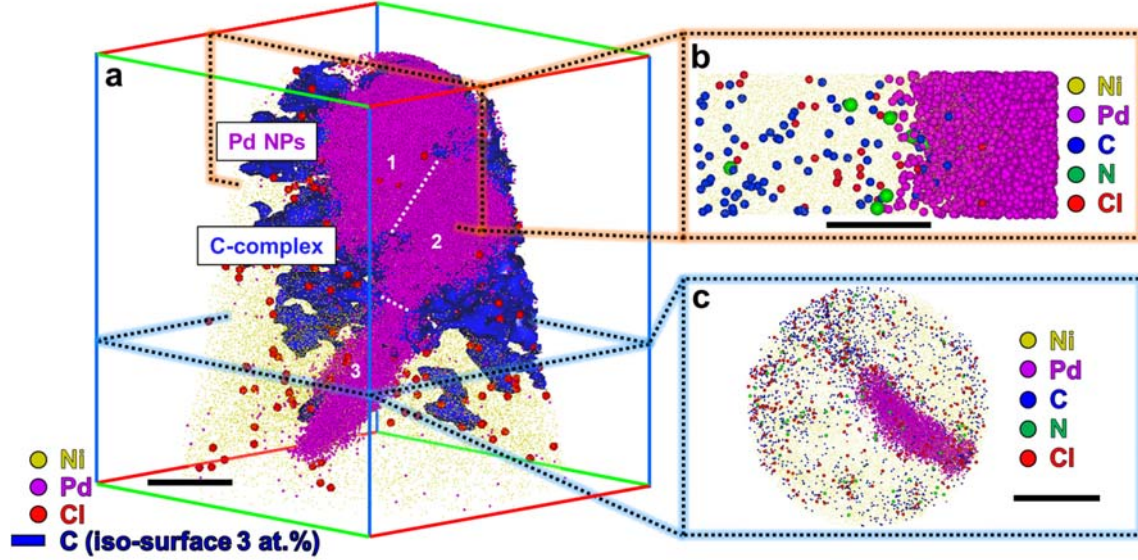


**Fig. 4 Atom probe tomography (APT) reconstruction of Pd nanoparticles (NPs), synthesized by adding Cl anions, embedded in Ni. a** Three-dimensional atom map of Pd atoms and isoconcentration (3 at.%) surfaces of C; the white dotted lines indicate the boundaries of each NP. **b, c** Slices viewed along the Pd NPs. (Scale bars: 10 nm in **a**, 5 nm in **b**, 20 nm in **c**)

To quantify the amount of  $\text{CTA}^+$  adsorbed on the surfaces of the  $\text{Pd}_{(\text{Br})}$  and  $\text{Pd}_{(\text{Cl})}$  NPs, we calculated the Gibbsian interfacial excess of the C atoms at the Pd/Ni interface ( $\Gamma_C$ ). For a cylindrical region of interest (ROI) ( $\varnothing 5 \times 30 \text{ nm}^3$ ) aligned perpendicularly to a surface of a reconstructed Pd NP, the corresponding  $\Gamma_C$  can be expressed as<sup>44</sup>

$$\Gamma_C = \frac{1}{A\eta} N_C^{\text{excess}} = \frac{1}{A\eta} (N_C^{\text{total}} - N_C^{\text{Pd}} - N_C^{\text{Ni}}) \quad (1)$$

, where  $A$  and  $\eta$  are the cross-sectional area of the cylindrical ROI ( $4.91 \text{ nm}^2$ ) and the detection efficiency (37%) of the APT instrument<sup>45</sup>, respectively,  $N_C^{\text{excess}}$  is the excess number of C atoms at the Pd/Ni interface,  $N_C^{\text{total}}$  is the number of total C atoms in the ROI, and  $N_C^{\text{Pd}}$  and  $N_C^{\text{Ni}}$  are the numbers of C atoms in bulk Ni and Pd, respectively. Since  $N_C^{\text{Pd}}$  and  $N_C^{\text{Ni}}$  were below the

background noise level of the mass spectra of the Pd<sub>(Br)</sub> and Pd<sub>(Cl)</sub> NPs, we considered them to be zero for simplicity. The concentration of C impurities within the bare electrodeposited Ni films was just above the detection limit ( $0.010 \pm 0.005$  at%), and therefore, we assumed that all the C atoms originated from the CTA<sup>+</sup>. From the  $\Gamma_C$  value, we could derive the surface excess of CTA<sup>+</sup> on the Pd NPs ( $\Gamma_{\text{cetrimonium}}$ , in molecular ions per nm<sup>2</sup>) as follows

$$\Gamma_{\text{cetrimonium}} = \Gamma_C \times \frac{1 \text{ cetrimonium molecule}}{19 \text{ carbon atoms}} \quad (2)$$

, where the second factor indicates that one CTA<sup>+</sup> contains 19 C atoms. Eight cylindrical ROIs were placed along different directions with respect to a Pd<sub>(Br)</sub> NP to determine the local  $\Gamma_{\text{cetrimonium}}$  value. The resulting average was  $1.9 \pm 0.6$  CTA<sup>+</sup> per nm<sup>2</sup> of Pd<sub>(Br)</sub> NP surface.

The hydrophilic cationic head of a CTA<sup>+</sup> consists of one N atom and three methyl (CH<sub>3</sub>) groups and spans over an area of 0.64 nm<sup>2</sup><sup>46</sup>, indicating that 1.6 CTA<sup>+</sup> are required to completely cover 1 nm<sup>2</sup> of a Pd {111} surface on average. Thus, our findings indicate that the surface of a Pd<sub>(Br)</sub> NP can be completely covered with CTA<sup>+</sup>.

We could determine the  $\Gamma_{\text{cetrimonium}}$  value for the Pd<sub>(Cl)</sub> specimen in an identical manner for the regions where the C atoms were concentrated. The maximum value was 1.2 CTA<sup>+</sup> per nm<sup>2</sup>, indicating that the surface of a Pd<sub>(Cl)</sub> NP cannot be completely covered with CTA<sup>+</sup>, in contrast with the Pd<sub>(Br)</sub> NPs. These results imply that the type of halide ions used in the NP synthesis can influence the adsorption behavior of the surfactant molecules on the NPs. Moreover, the difference in the number density of CTA<sup>+</sup> on the particle surfaces explains why the Pd<sub>(Br)</sub> MTNPs showed remarkable stability whereas the Pd<sub>(Cl)</sub> NPs were prone to oxidative etching; the CTA<sup>+</sup> completely covered the surfaces of the Pd<sub>(Br)</sub> MTNPs, protecting them from being etched by oxidative reactants such as Cl<sup>-</sup>, OH<sup>-</sup>, and O<sub>2</sub> during their synthesis and storage.

**Theoretical discussion of the binding behavior of ligands on Pd NPs.** To validate the APT results and clarify the adsorption behavior of ligands on the studied Pd NPs, we performed DFT calculations. First, we calculated the surface energy for the low-indexed facets of pure Pd, i.e., the {100}, {110}, and {111} surfaces (Fig. 5a), observing an increase in the as-obtained values in the order of {111} (0.085 eV/Å<sup>2</sup>), {100} (0.094 eV/Å<sup>2</sup>), and {110} (0.101 eV/Å<sup>2</sup>), which well agrees with previous theoretical and experimental results<sup>47</sup>. Thus, if the shape of a Pd NP is determined only by its surface energy, the Wulff construction predicts that a Pd NP without any adsorbed ligands will form {111} and {100} facets<sup>35,48</sup>.

Next, we calculated the binding energy of the Br and Cl anions on each Pd facet in vacuum; regardless of the facet, Cl<sup>-</sup> exhibited stronger interaction with the Pd surfaces than Br<sup>-</sup> (Fig. 5b). A detailed analysis of the projected density of states (PDOS) showed that the p-orbitals of the halide ions were overlapped with the d-orbitals of the Pd surfaces, and this overlap was stronger for the Cl anions than the Br ones, forming stronger covalent bonds (Supplementary Fig. 7).

However, since the actual synthesis of Pd<sub>(Br)</sub> and Pd<sub>(Cl)</sub> NPs was performed in aqueous solutions, the binding behavior of the halide ions on Pd facets in an aqueous medium had to be considered. Hence, we derived the binding energy in solutions from the values for vacuum according to the Born–Haber cycle<sup>49</sup> (Supplementary Fig. 8). As shown in Fig. 5c, the Br anions showed stronger interactions with the Pd {100}, {110}, and {111} facets than the Cl ones. This result was mainly attributed to the lower solvation energy and electron affinity of Br<sup>-</sup> compared to Cl<sup>-</sup> (Fig. 5d,e)<sup>50</sup>, whose lower solvation energy is due to the larger ionic radii of Br<sup>-</sup> (Cl<sup>-</sup>: 1.81 Å; Br<sup>-</sup>: 1.96 Å)<sup>51</sup>.

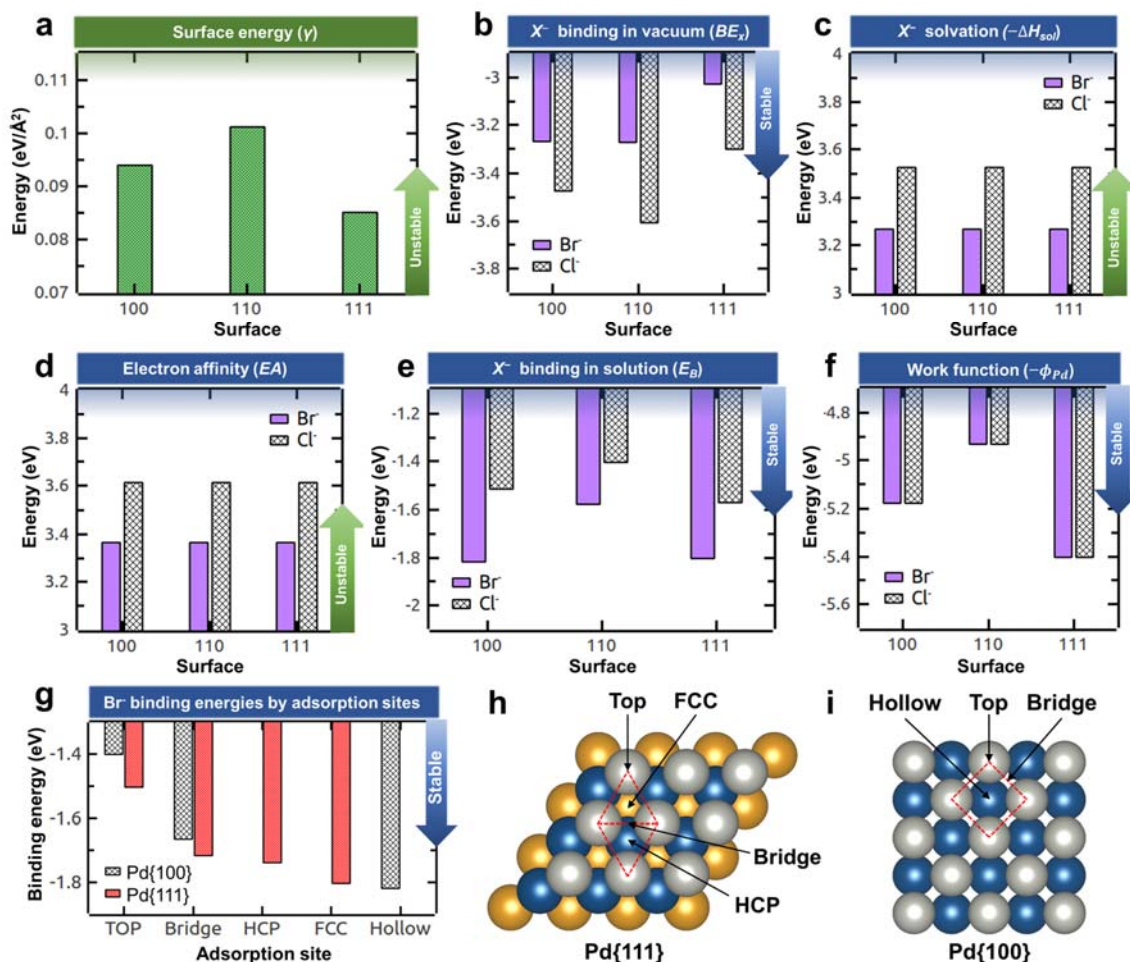


**Fig. 5 Density functional theory calculations.** **a** Surface energy values for Pd {100}, {110}, and {111} facets. **b** Binding energies of halide anions on Pd in vacuum. **c** Solvation energies of halide anions. **d** Electron affinities of halide anions. **e** Binding energies of halide anions on Pd in solutions. **f** Work functions of Pd surfaces. **g** Binding energies of Br<sup>-</sup> for the different adsorption sites of Pd surfaces; **h, i** Corresponding adsorption sites (face-centered cubic (FCC), hexagonal close-packed (HCP), bridge, and top) for Pd {111} and {100} facets from a top view.

Furthermore, the binding energy between Br<sup>-</sup> and Pd NPs was anisotropic. Figure 5e also shows that the Br anions bound more strongly to the {100} and {111} facets (-1.821 and -1.805 eV, respectively) than to the {110} ones (-1.579 eV) of Pd NPs in solutions, although the latter

ones exhibited the highest d-orbital center and, hence, were expected to be more reactive than the others (Supplementary Fig. 9). This contradictory result was attributed to the higher work function ( $\Phi_{\text{Pd}}$ ) values of the  $\{100\}$  and  $\{111\}$  (5.180 eV and 5.405 eV, respectively) than  $\{110\}$  surfaces (4.935 eV) (Fig. 5f), which led to higher stability compared to the  $\{110\}$  facets upon adsorbing  $\text{Br}^-$ . However, since the Pd  $\{111\}$  and  $\{100\}$  facets have similar surface energy and  $\text{Br}^-$  binding energy, the above considerations cannot fully explain the exclusive formation of  $\{111\}$  facets in  $\text{Pd}_{(\text{Br})}$  MTNPs.

To further clarify the adsorption behavior of  $\text{Br}^-$  on Pd, we calculated the binding energies of Br anions on different adsorption sites (face-centered cubic (FCC), hexagonal closed-packed (HCP), bridge, top, and hollow) of the Pd  $\{111\}$  and  $\{100\}$  surfaces (Fig. 5g). For the  $\{111\}$  facets, we identified four representative adsorption sites, i.e., FCC, HCP, bridge, and top (Fig. 5h)<sup>52,53</sup>. The binding strength increased in the following order: top (−1.504 eV) < bridge (−1.717 eV) < HCP (−1.741 eV) < FCC (−1.805 eV). For the  $\{100\}$  facets, we found three representative adsorption sites, that is, hollow, bridge, and top (Fig. 5i)<sup>52,53</sup>, and the binding strength increased as follows: top (−1.400 eV) < bridge (−1.667 eV) < hollow (−1.821 eV). The PDOS analysis revealed that these site-specific variations of binding strength for both facets were related to the covalent degree of the bonding between Pd surface and  $\text{Br}^-$  through the overlap of the p-orbitals of the latter and the d-orbitals (especially the  $d_{xz}$  and  $d_{yz}$  orbitals) of the former (Supplementary Fig. 10). These results indicate that the Pd  $\{111\}$  facets comprise more energetically favorable adsorption sites than the  $\{100\}$  ones and, thus, can accommodate a larger number of Br anions.



## Discussion.

The different adsorption behavior of  $\text{CTA}^+$  on the  $\text{Pd}_{(\text{Br})}$  and  $\text{Pd}_{(\text{Cl})}$  NPs can be ascribed to the different interactions of  $\text{Br}^-$  and  $\text{Cl}^-$  with the Pd surfaces. The halide anions locally chemisorbed to a Pd surface usually form a negatively charged layer, attracting positively charged  $\text{CTA}^+$  and forming bonds with them via electrostatic interactions<sup>47,54,55</sup>. The DFT results showed (Fig. 5e) that the Br anions can be adsorbed on the Pd surfaces with a higher density than the Cl ones in solution; we also found that  $\text{Br}^-$  can promote more  $\text{CTA}^+$  adsorption than  $\text{Cl}^-$ , consistent with previous molecular dynamics simulations for Au surfaces<sup>56,57</sup>.

A comparative analysis of the  $\text{Br}^-$  binding energy for various adsorption sites on the Pd {111} and {100} facets (Fig. 5g) suggested that the {111} surfaces exhibit the highest number density of adsorption sites. Therefore, the  $\text{Br}^-$  layers formed on a {111} surface are expected to show a higher charge density than those formed on a {100} facet, allowing a higher density of bonds with  $\text{CTA}^+$ . Since the cationic heads and the alkyl tails of  $\text{CTA}^+$  are hydrophilic and hydrophobic, respectively, the  $\text{CTA}^+$  may be adsorbed on the Pd surfaces via their cationic heads and form a double layer with the cationic heads of the second layer facing outward (Fig. 6)<sup>58</sup>. The  $\text{Br}^-$  layer formed on the  $\text{Pd}_{(\text{Br})}$  NP surfaces not only exerts an attractive electrostatic force on  $\text{CTA}^+$  but may also partly screen the electrostatic repulsion between the cationic heads of  $\text{CTA}^+$ , enhancing their surface excess<sup>58,59</sup>. Thus, the high density of adsorbed  $\text{CTA}^+$  stabilizes the {111} facets, in particular for the  $\text{Pd}_{(\text{Br})}$  MTNPs (Fig. 6). Moreover,  $\text{Br}^-$  and  $\text{CTA}^+$  may reduce the growth rate of the MTNPs, suppressing their evolution into single-crystal NPs<sup>35</sup>.

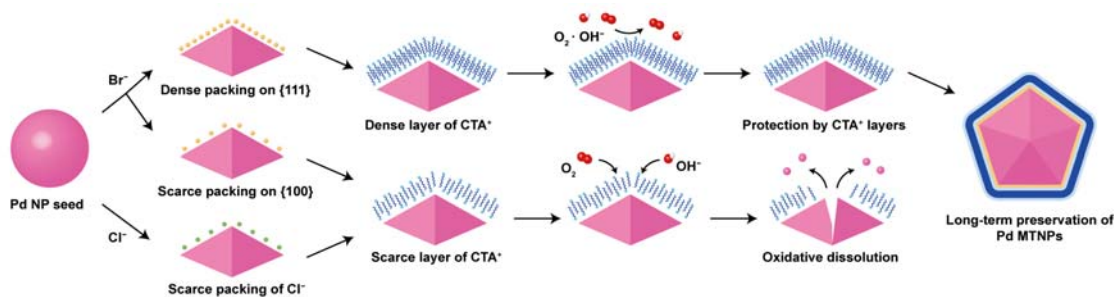


**Fig. 6 Influence of halide anions and cetrimonium ions (CTA<sup>+</sup>) on the shape and oxidation stability of Pd nanoparticles (NPs) and multiple-twinned nanoparticles (MTNPs).**

These mechanisms explain why the MTNPs, comprising {111} facets only, were the major product with Br<sup>-</sup> and CTA<sup>+</sup> for Pd<sub>(Br)</sub>. We noted that the joint addition of Br<sup>-</sup> and CTA<sup>+</sup> is the key to the synthesis of MTNPs. As in our case, a previous study demonstrated that Au–Pd NPs with {111} facets could be synthesized by using both Br<sup>-</sup> and CTA<sup>+</sup> in aqueous solutions<sup>60</sup>, whereas the addition of Br<sup>-</sup> alone can promote the formation of the {100} facets of noble metal NPs<sup>34,35</sup>. These results indicate that the shape control of noble metal NPs by Br<sup>-</sup> addition cannot be ascribed only to the ligand ion species but to the overall chemical environment during the NP synthesis, including the interactions between different ligands, as well as between ligand and solvent molecules, besides the adsorption behavior of the ligand ions on the NP surfaces.

Moreover, a different ligand adsorption behavior explains why the Pd<sub>(Br)</sub> NPs exhibited substantially higher resistance to oxidative etching than the Pd<sub>(Cl)</sub> ones. Capping ligands can protect MTNPs against oxidative attack by covering their surfaces<sup>33,61</sup>; our findings support this mechanism (Fig. 6). The detected number density of CTA<sup>+</sup> on Pd<sub>(Cl)</sub> NPs was insufficient to form a monolayer, while the CTA<sup>+</sup> fully covered the surfaces of the Pd<sub>(Br)</sub> NPs. Thus, the Pd<sub>(Cl)</sub> NPs were prone to oxidative etching, whereas the Pd<sub>(Br)</sub> MTNPs showed high stability even over long-term (ten days) storage in air.

In this work, we elucidated the adsorption and 3D distribution of ligands on colloidal Pd NPs via APT measurements and ab initio DFT calculations. We clarified the binding nature of ligands and the interplay between halide ions ( $\text{Br}^-$  and  $\text{Cl}^-$ ) and  $\text{CTA}^+$ , which are among the most commonly used ligands in colloidal synthesis. We revealed that  $\text{Br}^-$  forms stronger covalent bonds with Pd than  $\text{Cl}^-$  and enhances the adsorption of  $\text{CTA}^+$  on the Pd NPs through electrostatic interactions. The surface excess of  $\text{CTA}^+$  was higher than the value required to form a monolayer when synthesizing Pd NPs with  $\text{Br}^-$  addition, stabilizing the Pd {111} facets and multiple-twinned structures and enhancing the resistance of the Pd MTNPs against oxidative etching.

Finally, the direct imaging of ligands, as demonstrated here, should be extended to other systems to provide a general understanding of the ligand adsorption on NPs. This is essential for the knowledge-based tailoring of physical and electrochemical properties of NPs for specific target applications.

## Methods

**Chemicals.** Potassium tetrachloropalladate (II) ( $\text{K}_2\text{PdCl}_4$ , 98 %), potassium bromide (KBr, 99 %), potassium chloride (KCl, 99 %), cetrimonium chloride (CTAC, Mw = 320.00, 25 wt. % in water), all purchased from Sigma Aldrich, were used for the synthesis of Pd NP. Nickel sulfate heptahydrate ( $\text{NiSO}_4 \cdot 6\text{H}_2\text{O}$ , Junsei Chemical Co.) and dihydrogen borate ( $\text{H}_3\text{BO}_3$ , Sigma Aldrich), and nickel chloride hexahydrate ( $\text{NiCl}_2 \cdot 6\text{H}_2\text{O}$ , Samchun Chemical Co.) were used for the electrodeposition process. Deionized (DI) water was used in all experiments.

**Synthesis of Pd nanoparticles.** Pd<sub>(Br)</sub> NPs were synthesized by using KBr. 13 mg of K<sub>2</sub>PdCl<sub>4</sub> (II), 48 mg of KBr, 0.1 ml of CTAC were dissolved in 7 ml of distilled water. K<sub>2</sub>PdCl<sub>4</sub> was used as a precursor, and the latter two chemicals were added as a shape-controlling agent and a surfactant, respectively. The prepared precursor solution was placed in an oven and kept at 90 °C for 48 h in air. During the reaction the solution color changed from turbid orange to black, indicating that the Pd precursor was reduced to form zero-valent Pd nanoparticles. Pd<sub>(Cl)</sub> NPs were synthesized by replacing KBr with KCl and dissolving 30 mg of KCl instead of KBr while maintaining the other synthesis conditions.

**Embedding Pd nanoparticles in a Ni matrix for APT sample preparation.** The Pd NPs were collected using a centrifuge (8000 rpm for 30 min) and re-dispersed in distilled water under ultrasonication for 30 min. This washing process was performed three times for removing excess amounts of CTAC from the solution and observing only the CTAC attached to the nanoparticles.

As-washed Pd NPs were electrodeposited within a Ni matrix according to the procedure developed by Kim et al<sup>39</sup>. The process consisted of two steps, namely electrophoresis of nanoparticles on a flat Cu substrate followed by electroplating of a Ni matrix.

A vertical cell with a Cu substrate placed at the bottom and a Pt electrode on top was used for both electrophoresis and electroplating using a potentiostat (WPG100e, WonATech). For electrophoresis, the Pd nanoparticle solution was poured into the cell and a constant current of 10 mA was applied for 100 s. Subsequently, the remaining nanoparticle solution was removed and replaced by a modified Watts solution for Ni plating<sup>62</sup>. Electrodeposition of Ni was carried out at a constant current of 100 mA for 200 s.

**Fourier transform infrared (FT-IR) spectroscopy analysis.** A Nicolet iS 50 FT-IR spectrometer (Thermo Scientific, USA) was used for the collection of spectra in the range from 400 to 3600  $\text{cm}^{-1}$  at a spectral resolution of 1.928  $\text{cm}^{-1}$ . The data analysis was carried out using the OMNIC software (Version 9.2.106, Thermo Scientific, USA).

**TEM and APT characterization.** As-synthesized nanoparticles were characterized with respect to their size distribution and morphology using TEM (Tecnai G2 F30 S-Twin) operated at 300 kV in conventional mode. Average particle sizes were determined from 100 nanoparticles randomly selected from TEM images. HAADF-STEM images were obtained on a FEI Talos F200X operated at 200 kV. TEM specimens were prepared by depositing a water-dispersed nanoparticle sample on a carbon-coated copper grid. Atom probe tomography (APT) specimens were prepared using FIB (Helios Nanolab 450, FEI) milling according to Ref<sup>41</sup>. APT measurements were done using a CAMECA LEAP<sup>TM</sup> 4000X HR system in pulsed-laser mode at a detection rate of 0.3 %, a base temperature of 65 K, a laser pulse energy of 50 – 60 pJ, and a pulse frequency of 125 kHz. Data reconstruction and analyses were performed using the commercial software, Imago visualization and analysis system (IVAS) 3.8.2 developed by CAMECA Instruments. All three-dimensional atom maps presented in this paper were reconstructed using the standard voltage reconstruction protocol<sup>64</sup>.

**DFT calculations.** Spin-polarized DFT calculations were performed within the generalized gradient approximation (GGA-PW91), as implemented in the Vienna Ab-initio Simulation Package (VASP)<sup>65</sup>. The projector augmented wave (PAW) method with a plane wave basis set was employed to describe the interaction between ion cores and valence electrons<sup>66</sup>. An energy cutoff of 400 eV was applied for the expansion of the electronic eigenfunctions. Supplementary

Fig. 11 shows the geometries of the surface models ( $\{100\}$ ,  $\{110\}$ , and  $\{111\}$  planes of Pd) used for the DFT calculations. For constructing the supercell, each model surface was separated from its periodic images in the vertical direction by a vacuum space corresponding to ten atomic layers. For the Brillouin zone integration of Pd (100), (110), and (111) surfaces, we used a  $(5 \times 5 \times 1)$  Monkhorst-Pack mesh of  $k$  points to determine the optimal geometries and total energies of systems<sup>67</sup>. For each surface model, all Pd atoms were fixed at corresponding bulk positions, while the adsorbate position was fully relaxed using the conjugate gradient method until residual forces on all the constituent atoms became smaller than  $5 \times 10^{-2}$  eV/Å. For the work function calculation, we increased the  $k$  point mesh to  $(10 \times 10 \times 1)$ .

The surface energy ( $E_{surf}$ ) of each facet was determined by the relation  $E_{surf} = \frac{E_{slab} - N\epsilon}{2A}$ , where  $N$  is the number of total Pd atoms in a simulation box,  $\epsilon$  is the cohesive energy per atom of the Pd bulk,  $E_{slab}$  is the total energy of the surface structure with vacuum, and  $A$  is the surface area.

According to the Born-Haber cycle approach (see Supplementary Fig. 10), the binding energy ( $E_B$ ) of a halide ion ( $X^-$ ) to a Pd surface is given as  $E_B = BE_x - \Delta H_{sol} - \Phi_{Pd} + EA_X$ , where  $BE_x$  is the binding energy for the adsorption of halogen atoms to a negatively charged Pd surface with one extra electron,  $\Delta H_{sol}$ ,  $\Phi_{Pd}$ , and  $EA_X$  are the solvation energy of  $X^-$  in liquid water, the work function of a corresponding Pd surface, and the electron affinity of  $X$ , respectively<sup>47</sup>. Here,  $BE_x$  is given as  $BE_x = E_{Pd-X} - E_s - E_X$ , where  $E_{Pd-X}$  is the energy of the negatively charged surface with the bound halogen atom,  $E_s$  is the energy of the bare Pd surface without any adsorbate but with one extra electron, and  $E_X$  is the energy of the neutral atom ( $X$ ). We assumed that the interaction between water and Pd before and upon  $X$  adsorption does not change.  $\Delta H_{sol}$  and  $EA_X$  values were taken from the reports by Marcus et al. and NIST, respectively<sup>68,69</sup>.

## **Contributions**

K.S.J. and S.H.K. designed the experiment, carried out chemical synthesis and characterization. H.S.J. and C.W.J carried out TEM analysis and FIB processing. K.S.J., S.H.K., H.S.J. and C.W.J conducted APT analysis and data processing. J.W.Y. and S.H.L. performed DFT calculations. All authors discussed the results and contributed to the manuscript writing under the supervision of P.P.C. and S.H.L.

## **Corresponding authors**

Correspondence to Sangheon Lee and Pyuck-Pa Choi.

\*Sangheon Lee

\*E-mail: [sang@ewha.ac.kr](mailto:sang@ewha.ac.kr)

\*Pyuck-Pa Choi

\*E-mail: [p.choi@kaist.ac.kr](mailto:p.choi@kaist.ac.kr)

## **Acknowledgement**

K.J., S.K., H.J., C.J., and P.C. acknowledge the support of the National Research Foundation of Korea (NRF) (NRF-2018R1A4A1022260) and of the KAIST Venture Research Program for Graduate & Ph.D. students. J.Y. and S.L. acknowledge the support of the Basic Science Research Program through the National Research Foundation (NRF) of Korea funded by the Ministry of Education (NRF-2018R1D1A1B07051430). S.K. acknowledges financial support from the ERC-CoG-SHINE-771602.

## References

1. Alivisatos, A. P. Semiconductor clusters, nanocrystals, and quantum dots. *Science* **271**, 933–936 (1996).
2. Coleman, J. N. *et al.* Two-dimensional nanosheets produced by liquid exfoliation of layered materials. *Science* **331**, 568–571 (2011).
3. Arico, A. S., Bruce, P., Scrosati, B., Tarascon, J. M., & Van Schalkwijk, W. Nanostructured materials for advanced energy conversion and storage devices. *Nat. Mater.* **4**, 366–377 (2005).
4. Xia, B. Y. *et al.* A metal-organic framework-derived bifunctional oxygen electrocatalyst. *Nat. Energy* **1**, 1–8 (2016).
5. Jin, R., Zeng, C., Zhou, M. & Chen, Y. Atomically Precise Colloidal Metal Nanoclusters and Nanoparticles: Fundamentals and Opportunities. *Chem. Rev.* **116**, 10346–10413 (2016).
6. Joo, S. H. *et al.* Thermally stable Pt/mesoporous silica core-shell nanocatalysts for high-temperature reactions. *Nat. Mater.* **8**, 126–131 (2009).
7. Smith, A. M., Mohs, A. M. & Nie, S. Tuning the optical and electronic properties of colloidal nanocrystals by lattice strain. *Nat. Nanotechnol.* **4**, 56–63 (2009).
8. Ning, Z. *et al.* Graded doping for enhanced colloidal quantum dot photovoltaics. *Adv. Mater.* **25**, 1719–1723 (2013).
9. Song, H. *et al.* Hydrothermal growth of mesoporous SBA-15 silica in the presence of PVP-stabilized Pt nanoparticles: Synthesis, characterization, and catalytic properties. *J. Am. Chem. Soc.* **128**, 3027–3037 (2006).
10. Xiong, Y., McLellan, J. M., Yin, Y. & Xia, Y. Synthesis of palladium icosahedra with twinned structure by blocking oxidative etching with citric acid or citrate ions. *Angew. Chemie - Int. Ed.* **46**, 790–794 (2007).



11. Shang, W. *et al.* Core–Shell Gold Nanorod@Metal–Organic Framework Nanoprobes for Multimodality Diagnosis of Glioma. *Adv. Mater.* **29**, (2017).
12. Hu, H. *et al.* Interfacial Synthesis of Highly Stable CsPbX<sub>3</sub>/Oxide Janus Nanoparticles. *J. Am. Chem. Soc.* **140**, 406–412 (2018).
13. Al-Hajaj, N. A. *et al.* Short ligands affect modes of QD uptake and elimination in human cells. *ACS Nano* **5**, 4909–4918 (2011).
14. Wu, Z. *et al.* Thiolate ligands as a double-edged sword for CO oxidation on CeO<sub>2</sub> supported Au<sub>25</sub>(SCH<sub>2</sub>CH<sub>2</sub>Ph)<sub>18</sub> nanoclusters. *J. Am. Chem. Soc.* **136**, 6111–6122 (2014).
15. Boles, M. A., Ling, D., Hyeon, T. & Talapin, D. V. The surface science of nanocrystals. *Nat. Mater.* **15**, 364 (2016).
16. Campisi, S., Schiavoni, M., Chan-Thaw, C. E. & Villa, A. Untangling the role of the capping agent in nanocatalysis: Recent advances and perspectives. *Catalysts* **6**, 1–21 (2016).
17. Heinz, H. *et al.* Nanoparticle decoration with surfactants: Molecular interactions, assembly, and applications. *Surf. Sci. Rep.* **72**, 1–58 (2017).
18. Wu, M. *et al.* Solution NMR Analysis of Ligand Environment in Quaternary Ammonium-Terminated Self-Assembled Monolayers on Gold Nanoparticles: The Effect of Surface Curvature and Ligand Structure. *J. Am. Chem. Soc.* **141**, 4316–4327 (2019).
19. Jackson, A. M., Myerson, J. W. & Stellacci, F. Spontaneous assembly of subnanometre-ordered domains in the ligand shell of monolayer-protected nanoparticles. *Nat. Mater.* **3**, 330–336 (2004).
20. Zhou, Q. *et al.* Real-space imaging with pattern recognition of a ligand-protected Ag<sub>374</sub> nanocluster at sub-molecular resolution. *Nat. Commun.* **9**, (2018).

21. Reetz, M. T. *et al.* Visualization of surfactants on nanostructured palladium clusters by a combination of STM and high-resolution TEM. *Science* **267**, 367–369 (1995).
22. Hao, X. *et al.* Direct Imaging for Single Molecular Chain of Surfactant on CeO<sub>2</sub> Nanocrystals. *Small* **14**, 1–7 (2018).
23. Son, J. G., Choi, E., Piao, Y., Han, S. W. & Lee, T. G. Probing organic ligands and their binding schemes on nanocrystals by mass spectrometric and FT-IR spectroscopic imaging. *Nanoscale* **8**, 4573–4578 (2016).
24. Malola, S. *et al.* A method for structure prediction of metal-ligand interfaces of hybrid nanoparticles. *Nat. Commun.* **10**, (2019).
25. Jahng, J. *et al.* Direct Chemical Imaging of Ligand-Functionalized Single Nanoparticles by Photoinduced Force Microscopy. *J. Phys. Chem. Lett.* **11**, 5785–5791 (2020).
26. Gault, B. A Brief Overview of Atom Probe Tomography Research. *Appl. Microsc.* **46**, 117–126 (2016).
27. Sun, X., Jiang, K., Zhang, N., Guo, S. & Huang, X. Crystalline Control of {111} Bounded Pt<sub>3</sub>Cu Nanocrystals: Multiply-Twinned Pt<sub>3</sub>Cu Icosahedra with Enhanced Electrocatalytic Properties. *ACS Nano* **9**, 7634–7640 (2015).
28. Huang, H. *et al.* Synthesis of Multiple-Twinned Pd Nanoparticles Anchored on Graphitic Carbon Nanosheets for Use as Highly-Active Multifunctional Electrocatalyst in Formic Acid and Methanol Oxidation Reactions. *Adv. Mater. Interfaces* **7**, 1–9 (2020).
29. Xiao, W. *et al.* Optimizing the ORR activity of Pd based nanocatalysts by tuning their strain and particle size. *J. Mater. Chem. A* **5**, 9867–9872 (2017).
30. Baletto, F., Ferrando, R., Fortunelli, A., Montalenti, F. & Mottet, C. Crossover among structural motifs in transition and noble-metal clusters. *J. Chem. Phys.* **116**, 3856–3863 (2002).

31. Choi, S. Il *et al.* A Comprehensive Study of Formic Acid Oxidation on Palladium Nanocrystals with Different Types of Facets and Twin Defects. *ChemCatChem* **7**, 2077–2084 (2015).
32. Song, M., Zhou, G., Lu, N., Lee, J., Nakouzi, E., Wang, H., & Li, D. Oriented attachment induces fivefold twins by forming and decomposing high-energy grain boundaries. *Science* **367**, 40–45 (2020).
33. Lim, B., Xiong, Y. & Xia, Y. A water-based synthesis of octahedral, decahedral, and icosahedral Pd nanocrystals. *Angew. Chemie - Int. Ed.* **46**, 9279–9282 (2007).
34. Peng, H. C., Xie, S., Park, J., Xia, X. & Xia, Y. Quantitative analysis of the coverage density of Br<sup>-</sup> ions on Pd{100} facets and its role in controlling the shape of pd nanocrystals. *J. Am. Chem. Soc.* **135**, 3780–3783 (2013).
35. Xiong, Y. & Xia, Y. Shape-controlled synthesis of metal nanostructures: The case of palladium. *Adv. Mater.* **19**, 3385–3391 (2007).
36. Hayat, S. S. *et al.* Nanoscale relaxation near twin-interfaces of palladium and platinum. *Indian J. Pure Appl. Phys.* **47**, 730–736 (2009).
37. Lim, B. *et al.* Shape-controlled synthesis of Pd nanocrystals in aqueous solutions. *Adv. Funct. Mater.* **19**, 189–200 (2009).
38. Borodko, Y., Jones, L., Lee, H., Frei, H. & Somorjai, G. Spectroscopic Study of Tetradecyltrimethylammonium Bromide Pt–C14TAB Nanoparticles: Structure and Stability. *Langmuir* **25**, 6665–6671 (2009).
39. Kim, S.-H. *et al.* A new method for mapping the three-dimensional atomic distribution within nanoparticles by atom probe tomography (APT). *Ultramicroscopy* **190**, 30–38 (2018).
40. Lim, J. *et al.* Atomic-Scale Mapping of Impurities in Partially Reduced Hollow TiO<sub>2</sub> Nanowires. *Angew. Chemie - Int. Ed.* **59**, 5651–5655 (2020).

41. Thompson, K. *et al.* In situ site-specific specimen preparation for atom probe tomography. *Ultramicroscopy* **107**, 131–139 (2007).
42. Audier, H. E., Milliet, A., Sozzi, G. & Denhez, J. P. The isomerization mechanism of alkylamines: Structure of  $[C_2H_6N]^+$  and  $[C_3H_8N]^+$  fragment ions. *Org. Mass Spectrom.* **19**, 79–81 (1984).
43. Barone, V., Lelj, F., Grande, P. & Russo, N. Structures and relative stabilities of  $[C_2H_6N]^+$  ions: A non-empirical and MNDO study. *J. Mol. Struct. THEOCHEM* **124**, 319–324 (1985).
44. Krakauer, B. W. & Seidman, D. N. Absolute atomic-scale measurements of the Gibbsian interfacial excess of solute at internal interfaces. *Phys. Rev. B* **48**, 6724–6727 (1993).
45. Larson, D. J., Prosa, T. J., Ulfing, R. M., Geiser, B. P. & Kelly, T. F. *Local Electrode Atom Probe Tomography. Local Electrode Atom Probe Tomography* (2013).  
doi:10.1007/978-1-4614-8721-0
46. Warr, G. G., Sen, R., Evans, D. F. & Trend, J. E. Microemulsion formation and phase behavior of dialkydimethylammonium bromide surfactants. *J. Phys. Chem.* **92**, 774–783 (1988).
47. Almora-Barrios, N., Novell-Leruth, G., Whiting, P., Liz-Marzán, L. M. & López, N. Theoretical description of the role of halides, silver, and surfactants on the structure of gold nanorods. *Nano Lett.* **14**, 871–875 (2014).
48. Wulff, G. XXV. Zur Frage der Geschwindigkeit des Wachstums und der Auflösung der Krystallflächen. *Zeitschrift für Krist. - Cryst. Mater.* **34**, 449–530 (1901).
49. Gómez-Díaz, J., Honkala, K. & López, N. A Density Functional Theory study on gold cyanide interactions: The fundamentals of ore cleaning. *Surf. Sci.* **604**, 1552–1557 (2010).

50. Magnussen, O. M. Ordered anion adlayers on metal electrode surfaces. *Chem. Rev.* **102**, 679–725 (2002).
51. Miessler, G.L.; Fischer, P.J.; Tarr, D. A. *Inorganic chemistry*. Pearson (2015).
52. Pašti, I. A. & Mentus, S. V. Halogen adsorption on crystallographic (1 1 1) planes of Pt, Pd, Cu and Au, and on Pd-monolayer catalyst surfaces: First-principles study. *Electrochim. Acta* **55**, 1995–2003 (2010).
53. Zhu, Q. & Wang, S. Trends and Regularities for Halogen Adsorption on Various Metal Surfaces. *J. Electrochem. Soc.* **163**, H796–H808 (2016).
54. Ghosh, S. & Manna, L. The Many ‘facets’ of Halide Ions in the Chemistry of Colloidal Inorganic Nanocrystals. *Chem. Rev.* **118**, 7804–7864 (2018).
55. Cheng, W., Dong, S. & Wang, E. Synthesis and Self-Assembly of Cetyltrimethylammonium Bromide-Capped Gold Nanoparticles. *Langmuir* **19**, 9434–9439 (2003).
56. Kumar Meena, S. *et al.* The role of halide ions in the anisotropic growth of gold nanoparticles: a microscopic, atomistic perspective. *Phys. Chem. Chem. Phys* **18**, 13246 (1324).
57. Da Silva, J. A., Dias, R. P., Da Hora, G. C. A., Soares, T. A. & Meneghetti, M. R. Molecular dynamics simulations of cetyltrimethylammonium bromide (CTAB) micelles and their interactions with a gold surface in aqueous solution. *J. Braz. Chem. Soc.* **29**, 191–199 (2018).
58. Stolaś, A., Darmadi, I., Nugroho, F. A. A., Moth-Poulsen, K. & Langhammer, C. Impact of Surfactants and Stabilizers on Palladium Nanoparticle–Hydrogen Interaction Kinetics: Implications for Hydrogen Sensors. *ACS Appl. Nano Mater.* **3**, 2647–2653 (2020).

59. Wang, Z. & Larson, R. G. Molecular dynamics simulations of threadlike cetyltrimethylammonium chloride micelles: Effects of sodium chloride and sodium salicylate salts. *J. Phys. Chem. B* **113**, 13697–13710 (2009).
60. Bower, M. M., Desantis, C. J. & Skrabalak, S. E. A quantitative analysis of anions and pH on the growth of bimetallic nanostructures. *J. Phys. Chem. C* **118**, 18762–18770 (2014).
61. Yuan, H. *et al.* Reshaping anisotropic gold nanoparticles through oxidative etching: The role of the surfactant and nanoparticle surface curvature. *RSC Adv.* **5**, 6829–6833 (2015).
62. Di Bari, G. A. Electrodeposition of Nickel. in *Modern Electroplating: Fifth Edition* 79–114 (2011). doi:10.1002/9780470602638.ch3
63. Miller, M. K., Russell, K. F., Thompson, K., Alvis, R. & Larson, D. J. Review of atom probe FIB-based specimen preparation methods. *Microsc. Microanal.* **13**, 428–436 (2007).
64. Bas, P., Bostel, A., Deconihout, B. & Blavette, D. A general protocol for the reconstruction of 3D atom probe data. *Appl. Surf. Sci.* **87–88**, 298–304 (1995).
65. Kresse, G. & Marsman, M. *VASP the GUIDE*. Vienna University of Technology (2012).
66. Blöchl, P. E. Projector augmented-wave method. *Phys. Rev. B* **50**, 17953–17979 (1994).
67. Blöchl, P. E., Jepsen, O. & Andersen, O. K. Improved tetrahedron method for Brillouin-zone integrations. *Phys. Rev. B* **49**, 16223–16233 (1994).
68. Marcus, Y. Thermodynamics of solvation of ions. Part 5. - Gibbs free energy of hydration at 298.15 K. *J. Chem. Soc. Faraday Trans.* **87**, 2995–2999 (1991).
69. Johnson, R. Computational Chemistry Comparison and Benchmark Database (CCCBDB), <https://cccbdb.nist.gov/> (2020).